

CELLS MODELED AS RING POLYMERS; COLLECTIVE MOTILITY IN 2D

A REPORT

*submitted in partial fulfillment of the requirements
for the award of the dual degree of*

Master of Science

in

PHYSICS

by

DEEPAK PRADHAN

(PH22C018)

Under the guidance of

PROF. P. B. SUNIL KUMAR



**DEPARTMENT OF PHYSICS
INDIAN INSTITUTE OF TECHNOLOGY MADRAS
CHENNAI - 600036**

CERTIFICATE

This is to certify that **Deepak Pradhan**, M.Sc (Physics), has worked on the project entitled '**Cells Modeled as Ring Polymers; Collective Motility in 2D**' under my supervision and guidance. The content of this report is original and has not been submitted elsewhere for the award of any academic or professional degree.

May 2024

Prof. P. B. Sunil Kumar
Advisor
Department of Physics
IIT MADRAS
Chennai-600036

ACADEMIC INTEGRITY AND COPYRIGHT DISCLAIMER

I hereby declare that this project is my own work and to the best of my knowledge, it contains no materials previously published or written by another person or substantial proportions of material that have been accepted for the award of any other degree at IIT MADRAS or any other educational institution, except where due acknowledgment is made in the document.

I certify that all copyrighted material incorporated into this document is in compliance with the Indian Copyright Act (1957). In addition, I have diligently used appropriate references throughout this thesis report to acknowledge and appreciate previous relevant work. Every effort has been made to credit original authors and researchers whose works have contributed to the development of this research.

Furthermore, I acknowledge that a paper titled "Collective motion of cells modeled as ring polymers" authored by Haosheng Wen, Yu Zhu, Chenhui Peng, P. B. Sunil Kumar, and Mohamed Laradji has been reproduced as part of this thesis and appropriate citation has been provided within the thesis document.

May 2024



Deepak Pradhan

PH22C018

IIT Madras

ACKNOWLEDGEMENT

First and foremost, I express my deepest gratitude to my advisor, Prof. P. B. Sunil Kumar for entrusting me with the opportunity to work on this M.Sc. project under his expert guidance in the fields of active matter, biophysics, and soft matter physics. His invaluable insights and direction have been instrumental in shaping the trajectory of my research.

I extend sincere thanks to the Complex Fluid Lab of IIT Madras for providing the essential computational resources crucial for this study.

I am also grateful to the faculty and staff of the Department of Physics at IIT Madras for fostering an excellent academic environment and for providing the necessary resources that have been pivotal in the successful completion of my project.

Special appreciation goes to Ms.Aathira Murali for her introduction to LAMMPS and her invaluable assistance during the initial stages of my project. Additionally, I want to thank my dedicated labmates: Ritu, Siji, Akash, and Suvendu, for their unwavering support throughout this enriching journey.

I am indebted to the LAMMPS forum on MatSci.org for serving as a valuable platform for engaging discussions and insights, significantly contributing to the advancement of my project.

My heartfelt thanks also extend to my family and friends for their constant support, encouragement, and understanding throughout my academic pursuits.

ABSTRACT

The collective motion of cells has implications ranging from wound healing to colony propagation. In this study, we model cells as ring polymers and use molecular dynamics simulations to investigate their behavior at large scales. We specifically examine the effects of motility force and density on the collective motion of cells. Our observations indicate that collective motion increases with both motility force and density. During collective motion, the cells' velocities are more likely to align than their polarities and the misalignment of polarities actually facilitates collective behavior. We also explore the effect of a semiflexible boundary on a group of cells, finding that the composite system exhibits vertical motion at lower packing fractions and persistent motion at higher packing fractions. The effect of the bending modulus is less clear, showing persistent motion for some time followed by fluctuations over longer timescales. The study gives insight into the collective behavior of cells in biological systems and their behavior under flexible confinement.

LIST OF FIGURES

1.1	Cellular Pott's Model Annu. Rev.Cond. Matter Phys. Vol. 11:77-101	3
1.2	Phase field model of collective cell motility [1]	5
1.3	Model for collection of cells, a is a collection of cells, b is the single cell,c is the collection of cells modelled as a network and d is a single cell modelled as a polyhedron[2]	7
3.1	Schematic of a ring polymer representing an epithelial cell.	14
4.2	Steadystate snapshots under Different Propulsion Forces by elongated cells	23
4.4	Steadystate snapshots under Different Propulsion Forces by circular cells	24
4.5	Average cluster size $\langle m \rangle$ Vs motility force for circular cells and elongated cells and $\rho = 0.3125$	25
4.6	Normalized cluster distribution of elongated cells at $\rho = 0.3125$ for various value of motility force	26
4.7	the steady-state cluster-size distribution $p(m)$ for various packing fraction of Myxococcus xanthus[3] inset is for active rods[4]	26
4.8	The steady-state cluster-size distribution $p(m_{\max})$ for elongated cells.	27
4.9	the steady-state cluster-size distribution $p(m)$ for packing fraction ($\rho = 0.1563$ and 0.3125) elongated cells(red and blue) , circular cells (green)	28

4.10	Vicsek order parameter, calculated using motility force for the case of elongated cells with $\rho = 0.3125$, elongated cells with $\rho = 0.1563$, and circular cells with $\rho = 0.3125$. The inset shows the susceptibility of the Vicsek order parameter.	30
4.11	Polar order parameter, calculated using motility force for the case of elongated cells with $\rho = 0.3125$, elongated cells with $\rho = 0.1563$, and circular cells with $\rho = 0.3125$. The inset shows the susceptibility of the Polar order parameter	31
4.12	Snapshots of cells, their velocities and their polarities respectively	32
4.13	Vicsek order parameter with density in case of elongated cells	33
4.14	Various stages of collision of two elongated cells, the arrows show the direction of velocities of the individual cells lines are the polar axis of the cells	33
4.15	Different background colours in the graph indicate different stages of collision, For blue is the pre-collision stage, yellow is the collision stage, green is the adhesion stage and purple is the separation stage	35
4.16	Various stages of collision of two elongated cells, the arrows show the direction of velocities of the individual cells lines are the polar axis of the cells	35
4.17	Various stages of collision of two elongated cells, the arrows show the direction of velocities of the individual cells lines are the polar axis of the cells	36
4.18	The number below each figure indicates the number of cells inside the boundary. For the lower packing fraction, it shows vertical motion while for the higher packing fraction, it shows a persistent motion.	38
4.19	40
4.19	MSD plot of the confined active particles with time for various values of the bending modulus of the boundary	41

CONTENTS

Certificate	i
Academic Integrity and Copyright Disclaimer	ii
Acknowledgement	iii
Abstract	iv
List of Figures	vi
1. Introduction	2
1.1 Cellular pot model	2
1.2 Phase field Model	4
1.3 Network based model	6
1.4 Vicsek Model	6
1.5 Freely Jointed Chain	9
1.5.1 Persistence length	10
2. Molecular Dynamics Simulation and Programming tool . .	11
3. Methods	14
3.1 Model Description	14
3.1.1 Bonding energy	14
3.1.2 Bending energy	15
3.1.3 Area constraint	17
3.1.4 Propulsion force	18
4. Results	21

Contents	1
5. Summary and Outlook	42
Bibliography	45

1. INTRODUCTION

The cells move collectively in various examples of nature starting from cell development, cell regeneration, wound healing and also during metastasis. During collective cell motion, large no of cells move with equal speed and in the same direction.

The interaction of the cells as well as with the substrate plays an important role in the collective migration of cells. The types of force can be categorized as follows:- The collective motion of cells happens at a very low Reynolds number, which implies that we can easily neglect the inertial force on the cell. So the cell-substrate interaction can be modeled as an over-damped viscous force. In addition to the substrate, the cells exert a short-range repulsion force on each other. The cell shape compression is resisted by the elasticity of the cytoskeleton which gives rise to a compressibility factor to the area of each cell. The active forces generated by the molecular motors by the cells exert force on the substrate as a result the cells experience active stresses which lead to the collective motion. There are various models for collective cellular motion :

1.1 Cellular pot model

It is the extended version of the Monte-Carlo algorithm with metropolis dynamics applied to the Ising model. In this model, the cells are characterized by several domains in a large lattice, each lattice site as a subcellular part. Similar to the Ising model, each site can have values $N = 1, 2, 3, \dots, m$ equal to the no of cell types in the system. The state of each site is the updated using a Monte-Carlo scheme. The effective Hamiltonian for the cellular pots model

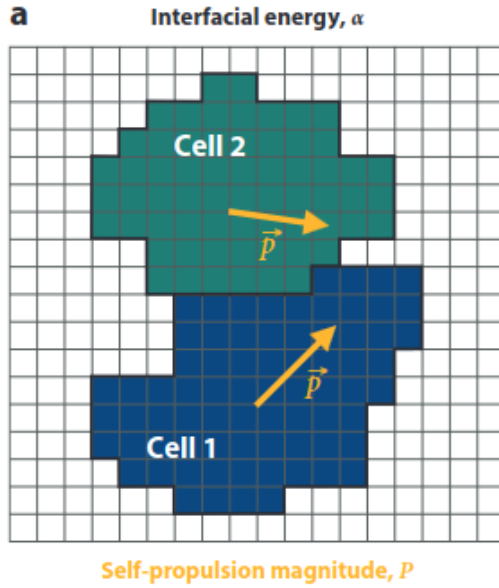


Fig. 1.1: Cellular Pott's Model Annu. Rev. Cond. Matter Phys. Vol. 11:77-101

is given by

$$\mathcal{H} = \sum_{(i,j)} J(\sigma_i, \sigma_j) + \lambda \sum_{\sigma=1}^{m-1} (A_\sigma - A_0)^2 - P \sum_{\sigma=1}^{m-1} \vec{R}_\sigma \cdot \vec{p}_\sigma. \quad (1.1)$$

The first term is the usual Hamiltonian term for Pott's model, $J(1 - \delta_{i,j})$ which accounts for the fluctuation in cells' shape, the second term accounts for the cell's area which penalizes if the area is not equal to A_0 . The last term decreases the energy of the cells if its centre of mass has a movement towards the polarity of the cells. This term is similar to the active polar forces in the cells.

The dynamics of lattice sites are done as follows :

1. A random lattice point is chosen in the lattice
2. Among the neighbours of that particular lattice point, choose a neighbour randomly and move that site to it.
3. Calculate the energy of the new system, if the energy is less than the

previous state, accept it.

4. If the energy is higher than the previous state accept the move by a probability of $\exp\left(\frac{\Delta U}{k_B T}\right)$. (ΔU is the energy difference between new state and previous state).

The cellular Pott's model does not explicitly include the viscous force by the substrate.

1.2 Phase field Model

In this model, the cell is represented by a field ϕ , and the value of ϕ is 0 outside the cell and 1 inside the cell. The equation of motion of the field is given by,

$$\frac{\partial \phi_i(\mathbf{x})}{\partial t} + \mathbf{v}_i(\mathbf{x}) \cdot \nabla \phi_i(\mathbf{x}) = -\frac{\delta \mathcal{F}}{\delta \phi_i(\mathbf{x})}, \quad (1.2)$$

Where the \mathcal{F} is the total free energy of the cells. The free energy of the cell can be written as,

$$\mathcal{F} = \mathcal{F}_{\text{CH}} + \mathcal{F}_{\text{area}} + \mathcal{F}_{\text{rep}} + \mathcal{F}_{\text{adh}} \quad (1.3)$$

$$\mathcal{F}_{\text{CH}} = \sum_i \frac{\gamma}{\lambda} \int d\mathbf{x} \left\{ 4\phi_i^2 (1 - \phi_i)^2 + \lambda^2 (\nabla \phi_i)^2 \right\}, \quad (1.4)$$

\mathcal{F}_{CH} represents the cahn-hilliard free energy of the cells. It keeps check on the deformability of the individual cells. The expression $\frac{\gamma}{\lambda}$ represents an energy scale with units of energy per unit area. The compressibility of the cells is taken into account by adding a free energy term which is proportional to its area and is given by,

$$\mathcal{F}_{\text{area}} = \sum_i \mu \int \left\{ 1 - \frac{1}{\pi R^2} \int d\mathbf{x} \phi_i^2 \right\}^2 d\mathbf{x} \phi_i^2, \quad (1.5)$$

Here μ is the strength of the constraint which restricts the area of the cell to πR^2 .

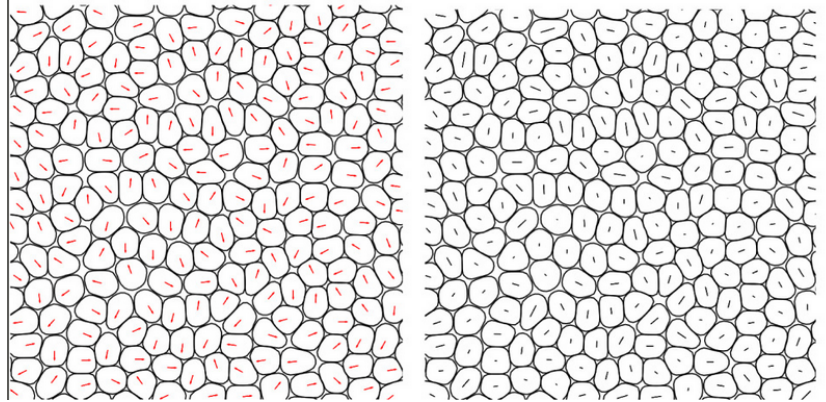


Fig. 1.2: Phase field model of collective cell motility [1]

The following terms account for the repulsion and adhesion between the cells,

$$\mathcal{F}_{\text{rep}} = \sum_i \sum_{j \neq i} \frac{\kappa}{\lambda} \int d\mathbf{x} \phi_i^2 \phi_j^2, \quad (1.6)$$

It penalizes the overlapping between the cells by an energy scale of $\frac{\kappa}{\lambda}$ having a unit of energy per unit area.

$$\mathcal{F}_{\text{adh}} = \sum_i \sum_{j \neq i} \omega \lambda \int \nabla \phi_i \cdot \nabla \phi_j d\mathbf{x}. \quad (1.7)$$

Here $\int d\mathbf{x} \nabla \phi_i \cdot \nabla \phi_j$ is the measure of the length of the contact line between two cells. $\frac{\omega}{\lambda}$ has units of energy per unit area.

Assuming overdamped dynamics.

$$\xi v_i(\mathbf{x}) = \mathbf{f}_i^{\text{tot}}(\mathbf{x}), \quad (1.8)$$

Here ξ is the friction coefficient and $\mathbf{f}_i^{\text{tot}}(\mathbf{x})$ is the total force acting on i th cell at position \mathbf{x} and $v_i(\mathbf{x})$ is the velocity of the i th cell.

The active forces on the cells is represented by,

$$\mathbf{f}_i^{\text{pol}}(\mathbf{x}) = \alpha \cdot \phi_i(\mathbf{x}) \cdot \mathbf{p}_i. \quad (1.9)$$

Where \mathbf{p}_i represents the polar axis of the cells and α is the parameter

controlling the activity of the cell.

The following can be a candidate for the polar axis to be chosen

1. The polar axis can be chosen to be in the same direction as the velocity or
2. The polar axis can be the elongation of the cell or
3. The orientation of the polar axis can do a random walk.

The phase field model is very useful while modelling the collection of cells at a very high density

1.3 Network based model

In the network-based model, the cell is modelled as a polyhedron with fixed thicknesss. The vertices and the edges of the cells are shared by the neighbouring cells. Each vertex in the network-based model is connected exactly to four edges. The faces of the polyhedron distinguish between the neighbours. The dynamics of the system are carried out by the motion of each vertex.

Collective motion in active matter

Active matter is a collection of self-propelled particles that take energy from the surrounding environment or they have their own stored energy and convert it into mechanical work. Many biological systems can be modelled as active matter starting from bacterial suspension to the school of fish in aquatic systems.

1.4 Vicsek Model

Vicsek model is one of the classic models showing the collective behaviour of active matter[5]. It consists of polar particles that can move in any direction. The particles reorient their velocity along the average direction of

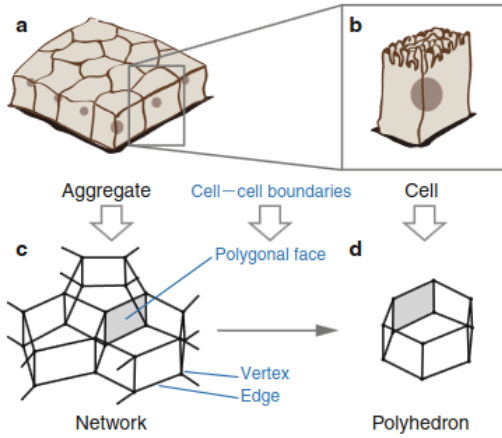


Fig. 1.3: Model for collection of cells, a is a collection of cells, b is the single cell,c is the collection of cells modelled as a network and d is a single cell modelled as a polyhedron[2]

propagation of particles in the neighbourhood of it and its perfect alignment is prevented due to some thermal noise. The phase transition in the Vicsek model is similar to that of the ferromagnetic transition. The magnetic field in the ferromagnetic case is analogous to the aligning interaction in the Vicsek model.

The Vicsek model consists of N particles each moving with a constant speed and having angle θ_j with the X axis in a square box with periodic boundary conditions. The velocity of the i th particle can be given by :

$$V_i = V_o * \exp(i\theta_i) \quad (1.10)$$

At each time step, each particle aligns itself along the average direction of the moving particles in its neighbourhood and there is a thermal noise that restricts itself from perfect alignment. The neighbourhood of a particle is defined by a circle of radius r , called interaction radius.

$$\theta_i(t + \Delta t) = <\theta_i(t)>_r + \Delta\theta \quad (1.11)$$

Where the $\Delta\theta$ is the thermal noise. The positions of the particles get

updated by :

$$X_i(t + \Delta t) = X_i(t) + V_i(t)\Delta t \quad (1.12)$$

The initial configuration was chosen to be a random orientation of the particles at different points. There are three parameters in this model, one is the number of active particles taken into account, the second is thermal noise and the third one is the propulsion velocity of the active particles. The phase transition from a random to a polar order state can be achieved by tuning the density as well as the noise in the model. The minimal noise and increase in the density of the active particles cause the phase transition to an ordered state.

For small values of noise and density, the active particles tend to form groups that move together but all the groups have velocities in different directions. For the higher values of both density and noise, the particles move randomly but with some correlation between them. But in the case of low noise and high density, the active particle starts moving in one direction causing a symmetry breaking. This type of phase transition is because the particle has constant velocity. The net momentum of this kind of system is not conserved. So a valid parameter to characterise the ordered state from the disordered state is the normalised average velocity of all the particles.

$$\mathbf{V}_a = \frac{1}{NV_o} \left| \sum_{i=1}^N \mathbf{V}_i \right| \quad (1.13)$$

The value of this order parameter is 0 if the particles are in a disordered state while the value approaches 1 as it moves to an ordered state.

POLYMERS

Polymers are long macromolecules consisting of repeating identical units. The structure and dynamics of the polymer are mainly governed by the collective behaviour of the monomers and the nature of the bond connecting them. Starting from DNA, and proteins to rubber and plastic. We modelled the cell as a ring polymer. Here is a brief overview of polymer dynamics.

1.5 Freely Jointed Chain

The simplest polymer one can think of consists of n bonds and all bonds are randomly oriented in all directions. This can be thought of as a path of a self-avoiding random walk of equal steps. This is known as the freely jointed chain. The Freely jointed chain is characterized by its end-to-end vector, $\vec{R} = \vec{R}_n - \vec{R}_o = \sum \vec{r}_i$. Where \vec{R}_i represents the position of the i th monomer while \vec{r}_i represents the i th bond.

Let us consider a freely jointed chain of bond length b , the orientation of each bond \vec{r}_i is chosen independently from some probability distribution $p(\vec{r}_i)$. After N steps $\vec{R} = \sum_{l=1}^N \vec{r}_i$ and the probability distribution of \vec{R} will be

$$\begin{aligned} P(\vec{R}, N) &= \int d\vec{r}_1 d\vec{r}_2 \dots d\vec{r}_N [p(\vec{r}_1)p(\vec{r}_2) \dots p(\vec{r}_N)] \delta \left(\vec{R} - \sum_{l=1}^N \vec{r}_i \right) \\ &= \int \prod_{l=1}^N [d\vec{r}_l p(\vec{r}_l)] \delta \left(\vec{R} - \sum_{l=1}^N \vec{r}_i \right). \end{aligned}$$

$$\begin{aligned} P(\vec{R}, N) &= \frac{1}{(2\pi)^3} \int d\vec{k} e^{i\vec{k}\cdot\vec{R}} \int \prod_{l=1}^N d\vec{r}_l p(\vec{r}_l) e^{-i\vec{k}\cdot\vec{r}_l} \\ &= \frac{1}{(2\pi)^3} \int d\vec{k} e^{i\vec{k}\cdot\vec{R}} [\bar{p}(\vec{k})]^N \quad \text{where} \\ \bar{p}(\vec{k}) &= \int d\vec{r} p(\vec{r}) e^{-i\vec{k}\cdot\vec{r}} \end{aligned}$$

$$\begin{aligned} \int d\vec{r} \exp(-i\vec{k}\cdot\vec{r}) p(\vec{r}) &= \frac{1}{4\pi b^2} \int_0^\infty dr r^2 \int_0^{2\pi} d\phi \int_0^\pi d\theta \sin \theta \exp(-ikr \cos \theta) \delta(r - b) \\ &= \frac{\sin kb}{kb} \end{aligned}$$

$$P(\vec{R}, N) = \frac{1}{(2\pi)^3} \int d\vec{k} e^{i\vec{k}\cdot\vec{R}} \left(\frac{\sin kb}{kb} \right)^N$$

If N is large, $((\sin kb)/kb)^N$ becomes very small unless kb is small. For $kb \ll 1$, $((\sin kb)/kb)^N$ can be approximated as

$$\left(\frac{\sin kb}{kb}\right)^N \simeq \left(1 - \frac{k^2 b^2}{6}\right)^N \simeq \exp\left(-\frac{Nk^2 b^2}{6}\right).$$

$$P(\vec{R}, N) = \frac{1}{(2\pi)^3} \int d\vec{k} e^{i\vec{k} \cdot \vec{R}} \exp\left(-\frac{Nk^2 b^2}{6}\right).$$

$$P(\vec{R}, N) = \left(\frac{3}{2\pi Nb^2}\right)^{3/2} \exp\left(-\frac{3\vec{R}^2}{2Nb^2}\right)$$

The distribution function of the end-to-end vector of a freely jointed chain is a gaussian.

1.5.1 Persistence length

In a polymer, the correlation between the tangent vectors at two different points separated by a distance r along the polymer contour which can be expressed by,

$$\langle \hat{t}(x) \cdot \hat{t}(x+r) \rangle = \exp \frac{-r}{A} \quad (1.14)$$

Here A is called the persistence length of a polymer.

2. MOLECULAR DYNAMICS SIMULATION AND PROGRAMMING TOOL

Our model is an approach to model the cell as a ring polymer and also to perform their molecular dynamics simulation. The basic idea of molecular dynamics simulation is to generate positions and velocities of several particles by integrating Newton's equations of motion taking into account specific interactions between them and studying the behaviour of their trajectories. The classical Hamiltonian of a system containing N number of particles $\{\mathbf{r}_1, \mathbf{r}_2, \dots, \mathbf{r}_N; \mathbf{p}_1, \mathbf{p}_2, \dots, \mathbf{p}_N\}$, where \mathbf{r}_i and $\mathbf{p}_i, i = 1, \dots, N$, are the coordinate and the momentum of particle i , and interacting via two-body, three-body as well as external forces, is given by:

$$\mathcal{H} = E_k + E_p = \sum_{i=1}^N \frac{p_i^2}{2m_i} + \sum_{i>j=1}^N V_2(r_{ij}) + \sum_{i=1}^N \sum_{j \neq i, k \neq i}^N V_3(\mathbf{r}_{ij}, \mathbf{r}_{ik}) + \dots + \sum_{i=1}^N V_{\text{ext}}(\mathbf{r}_i) \quad (2.1)$$

where E_k is the net kinetic energy of the system and E_p is the net potential energy of the system. $V_2(r_{ij})$ is the two-body interaction energy between particles i and j , separated by a distance $r_{ij} = |\mathbf{r}_i - \mathbf{r}_j|$.

$V_3(\mathbf{r}_{ij}, \mathbf{r}_{ik})$ is the three-body potential energy and $U_{\text{ext}}(r_i)$ is the external potential energy. m_i is the mass of the particle. Then the evolution of velocities and positions of the particles with time is given by:

$$\dot{r}_{i,\alpha} = \frac{\partial \mathcal{H}}{\partial p_{i,\alpha}} = \frac{p_{i,\alpha}}{m_i} \quad (2.2)$$

and

$$\dot{p}_{i,\alpha} = \frac{\partial \mathcal{H}}{\partial r_{i,\alpha}} = f_{i,\alpha} \quad (2.3)$$

with $\alpha = x, y$ or z . Then the above equations are integrated in time to get the trajectory of the particles. Basically, the time integration is the Taylor expansion of positions in small timesteps with Newton's laws of motion. the simplest time integration scheme is the truncation of the terms after the linear order, given by,

$$r(t + \Delta t) = r(t) + v(t)\Delta t + O(\Delta t^2) \quad (2.4)$$

This is called the Euler algorithm. This scheme has a numerical accuracy of the order $O(\Delta t^2)$. This is not a very efficient method for time integration, we have to choose very small timesteps to get any reasonable result.

The Verlet algorithm provides a more accurate time integration method. It is derived from the Taylor expansion by truncating the terms after the order (Δt^4) . The Taylor expansions is given by:-

$$\begin{aligned} r(t + \Delta t) &= r(t) + r'\Delta t + \frac{r''}{2}\Delta t^2 + \frac{1}{6}r'''(t) + O(\Delta t^4) \\ r(t - \Delta t) &= r(t) - r'\Delta t + \frac{r''}{2}\Delta t^2 - \frac{1}{6}r'''(t) + O(\Delta t^4) \end{aligned} \quad (2.5)$$

Adding the above two equations we get :

$$r(t + \Delta t) = 2r(t) - r(t - \Delta t) + \frac{r''}{2}\Delta t^2 + O(\Delta t^4) \quad (2.6)$$

The above equation is numerically accurate up to an order of $O(\Delta t^4)$ but there is a difficulty here: we have to store the positions of the previous timestep.

The Velocity verlet algorithm is used to integrate both the velocities and positions . the equations for the Velocity verlet algorithm are given by :

$$\begin{aligned} r(t + \Delta t) &= r(t) + v(t)\Delta t + \frac{f(t)}{2m}\Delta t^2 \\ v(t + \Delta t) &= v(t) + \frac{f(t) + f(t + \Delta t)}{2m}\Delta t \end{aligned} \quad (2.7)$$

With this algorithm, it is possible to calculate both kinetic and potential energy simultaneously. These equations are invariant under time reversal.

All the simulations in this project are done by LAMMPS[6]. The LAMMPS source code can be found at [link](#).

3. METHODS

3.1 Model Description

We consider a number of disjoint semiflexible ring polymers as our model of cells in two dimensions. Each is composed of 40 monomers in a good solvent. The ring polymer is a good example of epithelial cells in 2 dimensions. In our case, the ring consists of 40 beads. We define the polar axis of the ring polymer as the straight line connecting the 1st and 20th beads.[\[7\]](#)

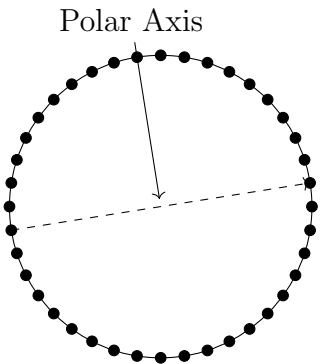


Fig. 3.1: Schematic of a ring polymer representing an epithelial cell.

3.1.1 Bonding energy

In our model, we represent each cell by projecting its boundary onto the xy-plane. This projection is approximated by a two-dimensional ring polymer composed of particles (beads) that are linearly bonded, as illustrated in [3.1](#). For this, utilize a simple quadratic potential energy between adjacent monomers i and $i + 1$:

$$U_{\text{bond}}(r_{i,i+1}) = \frac{k_{\text{bond}}}{2}(r_{i,i+1} - r_{\text{eq}})^2 \quad (3.1)$$

where $i = 1, \dots, N$, and the index $N + 1 \equiv 1$. In this equation, r_{eq} denotes the preferred bond length, $k_{\text{bond}} > 0$ represents the spring constant of the bond, and:

$$r_{i,i+1} = \sqrt{(x_{i+1} - x_i)^2 + (y_{i+1} - y_i)^2} \quad (3.2)$$

From the expression above, the elastic force along the α -th direction can be derived as:

$$F_{i,\alpha}^{\text{bond}} = -k_{\text{bond}}(r_{i,i+1} - r_{\text{eq}})(\alpha_{i+1} - \alpha_i) \quad (3.3)$$

$$= -\frac{\partial U_{\text{bond}}(r_{i,i+1})}{\partial \alpha_i}$$

where $\alpha = x$ or y , and $F_{i+1,\alpha}^{\text{bond}} = -F_{i,\alpha}^{\text{bond}}$.

3.1.2 Bending energy

The bending potential energy in our model is considered as a three-body interaction given by:

$$U_{\text{bend}}(\theta_i) = k_{i,\text{bend}}(1 - \cos \theta_i) \quad (3.4)$$

$$\cos \theta_i = \frac{\mathbf{r}_{i-1,i} \cdot \mathbf{r}_{i,i+1}}{r_{i-1,i} r_{i,i+1}} \quad (3.5)$$

Here θ_i is the angle of the triplet $(i - 1, i, i + 1)$. The role of this potential energy is to maintain the circular shape of the cell. For this kind of bending interaction, the preferred angle is 180° . The force due to this potential on the particles is given by:

$$\begin{aligned}
F_{i,\alpha}^{\text{bend}} &= -\frac{\partial}{\partial \alpha_i} U_{\text{bend}}(\theta_i) \\
&= -k_{i, \text{bend}} \left\{ \frac{(\alpha_{i+1} + \alpha_{i-1} - 2\alpha_i)}{r_{i,i+1} r_{i-1,i}} + \left[\frac{\alpha_i - \alpha_{i+1}}{r_{i,i+1}^3 r_{i-1,i}} + \frac{\alpha_i - \alpha_{i-1}}{r_{i,i+1} r_{i-1,i}^3} \right] \vec{r}_{i,i-1} \cdot \vec{r}_{i,i+1} \right\},
\end{aligned} \tag{3.6}$$

and the α -th components of the bending forces on particle $i+1$ and $i-1$ are respectively given by

$$\begin{aligned}
F_{i+1,\alpha}^{\text{bend}} &= -\frac{\partial}{\partial \alpha_{i+1}} U_{\text{bend}}(\theta_i) \\
&= k_{i, \text{bend}} \left[\frac{(\alpha_{i+1} - \alpha_{i+2})}{r_{i,i+1} r_{i+1,i+2}} + \frac{(\alpha_i - \alpha_{i+1})}{r_{i,i+1}^3 r_{i+1,i+2}} \vec{r}_{i,i+1} \cdot \vec{r}_{i+1,i+2} \right],
\end{aligned} \tag{3.7}$$

and

$$\begin{aligned}
F_{i-1,\alpha}^{\text{bend}} &= -\frac{\partial}{\partial \alpha_i} U_{\text{bend}}(\theta_i) \\
&= k_{i, \text{bend}} \times \left[\frac{(\alpha_{i-1} - \alpha_{i-2})}{r_{i,i-1} r_{i-1,i-2}} + \frac{(\alpha_i - \alpha_{i-1})}{r_{i,i-1}^3 r_{i-1,i-2}} \vec{r}_{i,i-1} \cdot \vec{r}_{i-1,i-2} \right]
\end{aligned} \tag{3.8}$$

To accommodate the polarity of the cell, triplets of monomers centred around monomers indexed at 1 and $N/2$ exhibit a preferred bending angle other than 180° . By changing this angle we can control the aspect ratio of each cell.

$$U_{\text{bend}}(\theta_i) = \frac{k_{i,\text{bend}}}{2} (\cos \theta_i - \cos \theta_{eq})^2 (\delta_{i,1} + \delta_{i,N/2}) \tag{3.9}$$

where $k_{\text{bend}} > 0$ is the bending elasticity coefficient related to the bending modulus of the cell's plasma membrane. θ_{eq} is the preferred angle, typically chosen as 180° , and θ_i is the angle of the triplet $(i-1, i, i+1)$ defined by:

$$\cos \theta_i = \frac{\mathbf{r}_{i-1,i} \cdot \mathbf{r}_{i,i+1}}{r_{i-1,i} r_{i,i+1}} \tag{3.10}$$

From Eq. (3.9), the α -th component of the force resulting from the bending potential energy on particle i is then given by:

$$\begin{aligned} F_{i,\alpha}^{\text{bend}} &= -\frac{\partial}{\partial \alpha_i} U_{\text{bend}}(\theta_i) \\ &= k_{i, \text{bend}} (\cos \theta_i - \cos \theta_{eq}) \\ &\quad \left\{ \frac{(\alpha_{i+1} + \alpha_{i-1} - 2\alpha_i)}{r_{i,i+1} r_{i-1,i}} + \left[\frac{\alpha_i - \alpha_{i+1}}{r_{i,i+1}^3 r_{i-1,i}} + \frac{\alpha_i - \alpha_{i-1}}{r_{i,i+1} r_{i-1,i}^3} \right] \vec{r}_{i,i-1} \cdot \vec{r}_{i,i+1} \right\}, \end{aligned} \quad (3.11)$$

and the α -th components of the bending forces on particle $i+1$ and $i-1$ are respectively given by:

$$\begin{aligned} F_{i+1,\alpha}^{\text{bend}} &= -\frac{\partial}{\partial \alpha_{i+1}} U_{\text{bend}}(\theta_i) = \\ &k_{i, \text{bend}} (\cos \theta_i - \cos \theta_{eq}) \left[\frac{(\alpha_{i+1} - \alpha_{i+2})}{r_{i,i+1} r_{i+1,i+2}} + \frac{(\alpha_i - \alpha_{i+1})}{r_{i,i+1}^3 r_{i+1,i+2}} \vec{r}_{i,i+1} \cdot \vec{r}_{i+1,i+2} \right], \end{aligned} \quad (3.12)$$

and

$$\begin{aligned} F_{i-1,\alpha}^{\text{bend}} &= -\frac{\partial}{\partial \alpha_{i-1}} U_{\text{bend}}(\theta_i) = \\ &k_{i, \text{bend}} \times (\cos \theta_i - \cos \theta_{eq}) \left[\frac{(\alpha_{i-1} - \alpha_{i-2})}{r_{i,i-1} r_{i-1,i-2}} + \frac{(\alpha_i - \alpha_{i-1})}{r_{i,i-1}^3 r_{i-1,i-2}} \vec{r}_{i,i-1} \cdot \vec{r}_{i-1,i-2} \right] \end{aligned} \quad (3.13)$$

3.1.3 Area constraint

The area constraints of the cells are accounted for by an additional effective potential energy given by:

$$\mathcal{U}_{\text{area}} = \frac{1}{2} \chi A_0 \left(1 - \frac{A}{A_0} \right)^2 \quad (3.14)$$

Here χ is the area strength modulus and A_0 is the preferred area of the cell, as the perimeter of the cell is fixed, so for a particular aspect ratio, we can calculate this preferred area.

The area of the individual cell is calculated through the shoelace formula, which is used to calculate the area of a polygon:

$$A = \frac{1}{2} \sum_{i=1}^n (x_i y_{i+1} - x_{i+1} y_i) = \frac{1}{2} \sum_{i=1}^n \begin{vmatrix} x_i & x_{i+1} \\ y_i & y_{i+1} \end{vmatrix} \quad (3.15)$$

where x_i and y_i are the coordinates of the i th bead of the cell.

The force experienced by the i th bead is given by:

$$F_{i,x}^{\text{Area}} = -\frac{\partial}{\partial x_i} U_{\text{Area}}(x_i, y_i) = \chi \left(1 - \frac{A}{A_0}\right) (y_{i-1} - y_{i+1}) \quad (3.16)$$

$$F_{i,y}^{\text{Area}} = -\frac{\partial}{\partial y_i} U_{\text{Area}}(x_i, y_i) = \chi \left(1 - \frac{A}{A_0}\right) (x_{i+1} - x_{i-1}) \quad (3.17)$$

3.1.4 Propulsion force

We define the line joining the first and $N/2$ th bead as our polar axis is decoupled from the long axis of the cell.

The propulsion of a cell, \mathbf{P}_l , is due to a non-conservative motility force, of magnitude F_D , and in the direction of the cell's polarity, $\mathbf{P}_l = \mathbf{r}_{l1} - \mathbf{r}_{l2}$, where l_1 and l_2 are the indices of the cell's poles.

$$\mathbf{f}_l(t) = F_D \frac{\mathbf{P}_l(t)}{P_l(t)} g(\bar{\mathbf{v}}_l(t), \mathbf{P}_l(t)), \quad (3.18)$$

where $g(\bar{\mathbf{v}}_l(t), \mathbf{P}_l(t))$ in Eq. (3.18) is defined as follows:

$$g(\bar{\mathbf{v}}_l(t), \mathbf{P}_l(t)) = \begin{cases} +1 & \text{if } \bar{\mathbf{v}}_l(t) \cdot \mathbf{P}_l(t) > 0 \\ -1 & \text{if } \bar{\mathbf{v}}_l(t) \cdot \mathbf{P}_l(t) < 0 \end{cases}$$

Here, $\bar{\mathbf{v}}_l(t)$ is the average velocity of the cell in the last τ_m timesteps.

$$\bar{\mathbf{v}}_l(t) = \frac{1}{\tau_m} \int_{t-\tau_m}^t \mathbf{v}_l(t') dt' \quad (3.19)$$

This propulsion force ensures that our self-propelled cell has a sustained memory for a definite amount of time and it can reverse its direction without being rotated.

There is no explicit aligning interaction force between the cells. In this model, the cells' boundaries are semiflexible also here it accounts for the volume enclosed by the cell by the area constraint.

In our study, we considered two kinds of self-propelled cells: one circular and the other elongated. The shape of the cells can be controlled by the bending potential we have at the poles of each cell (3.9) and the preferred area of the cells. For the circular cells, we choose the preferred angle to be 180° and assign A_o in (3.14) as the area of a perfect circle. For the elongated cells, we choose the angle to be 120° and use A_o in (3.14) as the area of an ellipse with the same polar angle, e.g., 120° .

The monomers of each cell move following a molecular dynamics scheme:

$$\begin{aligned} \dot{\mathbf{r}}_i(t) &= \mathbf{v}_i(t) && \text{and} \\ \mu \dot{\mathbf{v}}_i(t) &= -\nabla_i \mathcal{U} + \frac{1}{N} \mathbf{f}_l(t) - \frac{\mu}{\tau} \mathbf{v}_i(t) + \sqrt{\frac{2m k_B T}{\tau}} \Xi_i(t) \end{aligned} \quad (3.20)$$

where $\mathcal{U} = \mathcal{U}_{\text{bond}} + \mathcal{U}_{\text{bend}} + \mathcal{U}_{\text{rep}} + \mathcal{U}_{\text{area}}$, \mathbf{v}_i is the instantaneous velocity of monomer i , and l is the index of the cell to which i belongs. In eqn (19), μ is the mass of a monomer, $1/\tau$ is the friction coefficient, k_B is the Boltzmann constant and T is the temperature in the ideal case (i.e. in the absence of interactions), and $\Xi_i(t)$ is a random vector that has zero-mean and is δ -correlated for the same particle and same component, i.e. $\Xi'(t)$ satisfies

$$\begin{aligned} \langle \Xi_i(t) \rangle &= 0 \\ \langle \Xi_{i,\xi}(t) \Xi_{j,\zeta}(t') \rangle &= \delta_{ij} \delta_{\xi\zeta} \delta(t - t'), \end{aligned} \quad (3.21)$$

Where ξ and ζ represent either the coordinates x or y , δ_{nm} is the Kronecker delta, and $\delta(t)$ is the Dirac delta function.

The equations of motion are integrated using the velocity-Verlet algorithm

with a time step $\Delta t = 0.01\tau$, where $\tau = r_b \sqrt{\frac{\mu}{\varepsilon}}$. Here, r_b is the length scale and ε is an arbitrary energy scale. $\Xi_i(t)$ is a uniform distribution from -0.5 to 0.5 . Each cell is composed of $N = 40$ monomers. The values of the parameters of the model for elongated cells are,

$$\begin{aligned} k &= 200\varepsilon/r_b^2, \\ k &= 100\varepsilon, \\ \kappa' &= 1000\varepsilon \\ \theta_p &= 120^\circ \\ \varsigma &= 50\varepsilon \\ r_c &= r_b \\ \chi &= 1\varepsilon/r_b^2 \\ A_0 &= 88.10r_b^2 \\ \tau_m &= \tau \\ K_B T &= 1\epsilon \end{aligned}$$

In circular cells, the model parameters are the same as those for elongated cells, except that in this case, $\theta_p = 180^\circ$ and $A_0 = 127r_b^2$. With the parameters specified above, the aspect ratio of elongated cells is about 3.2, whereas that of circular cells is about 1.

The simulations are conducted in the NAT ensemble on systems with linear size $L_x = L_y = 400r_b$, utilizing periodic boundary conditions along both the x- and y-axes. The amplitude of the motility force is varied between 0 and $48\varepsilon/r_b$.

The cell density, defined as the ratio of the number of cells to the total area, is adjusted in the case of elongated cells within the range of 1.5625×10^{-2} to 0.3125, whereas for circular cells, it remains fixed at 0.3125.

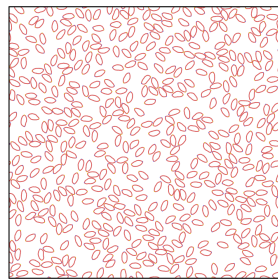
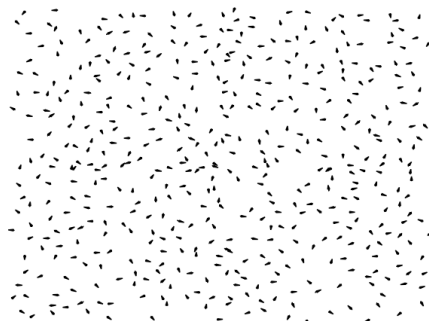
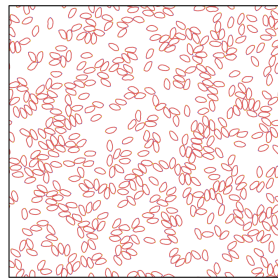
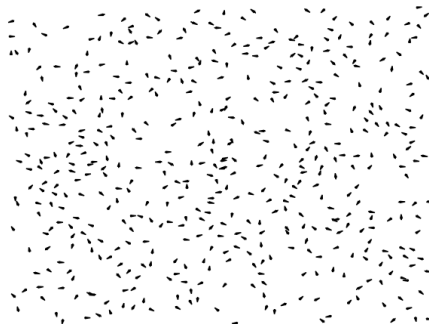
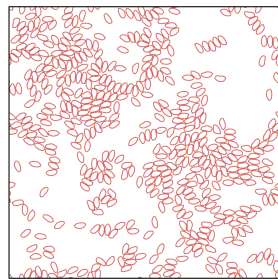
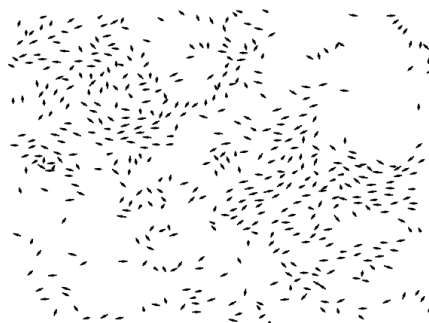
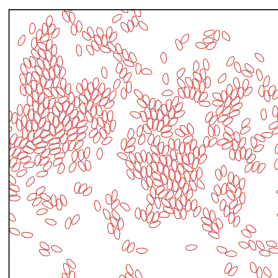
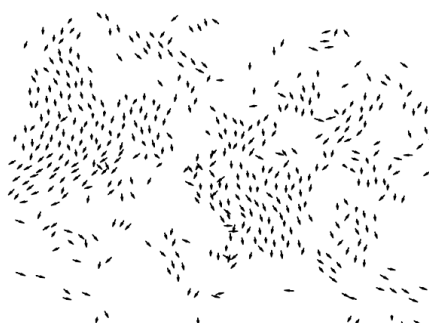
The value of the bending modulus κ' is taken to be 10 times that of κ , to have the same persistence length in both cases. This collective behaviour of cells has been studied before [7].

4. RESULTS

The investigation focuses on examining how changes in the motility force affect the collective migration behavior of cells. Specifically, the study maintains a constant number of cells while varying the motility force across a range from 0 to $\frac{40\epsilon}{r_b}$. The analysis centers on observing cluster formation, with the packing fraction of elongated cells held constant at $\rho = 0.3125$, while altering the propulsion force to $F_D = 0, 16, 24, 32, 40\frac{\epsilon}{r_b}$.

The qualitative findings suggest a clear relationship between the motility force and cluster formation. As the motility force increases, there is a notable augmentation in cluster formation among the cells. This effect becomes particularly conspicuous following the application of a motility force of $F_D = 16\frac{\epsilon}{r_b}$ or higher. Increasing the motility force enhances the ability of individual cells to move and interact with one another, leading to a higher tendency for them to form clusters or aggregates. Additionally, beyond $F_D = 30\frac{\epsilon}{r_b}$, an increase in motility force correlates with higher velocity coherence among the cells within the clusters.

The effect of cell shape emerges as a crucial factor in collective migration. Circular cells exhibit a reduced propensity to form clusters compared to elongated cells. This disparity is attributed to the lower activity-mediated cell-cell adhesion observed in circular cells compared to elongated ones, as evident from the figures. While circular cells do form clusters as activity increases, the velocities of cells within these clusters exhibit less correlation. Conversely, elongated cells demonstrate more coherent collective motion, emphasizing the significance of cell shape in governing collective migration dynamics. These findings underscore the intricate interplay between motility force, cell shape, and collective migration behaviour. There is a similar result where elongated active particles result in more collective motion [8].

(a) $F_D = 0 \frac{\epsilon}{r_b}$ (b) Velocity field for $F_D = 0 \frac{\epsilon}{r_b}$ (c) $F_D = 16 \frac{\epsilon}{r_b}$ (d) Velocity field for $F_D = 16 \frac{\epsilon}{r_b}$ (e) $F_D = 24 \frac{\epsilon}{r_b}$ (f) Velocity field for $F_D = 24 \frac{\epsilon}{r_b}$ (g) $F_D = 32 \frac{\epsilon}{r_b}$ (h) Velocity field for $F_D = 32 \frac{\epsilon}{r_b}$

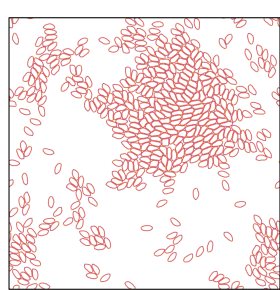
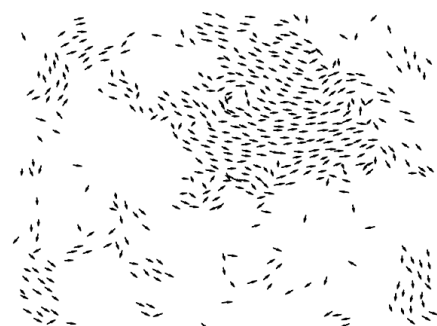
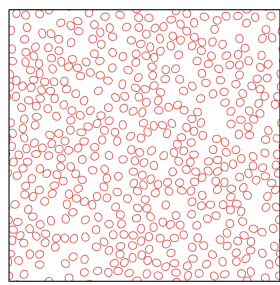
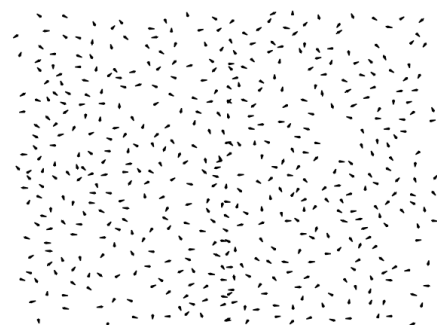
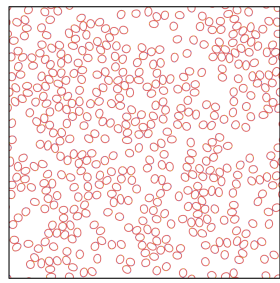
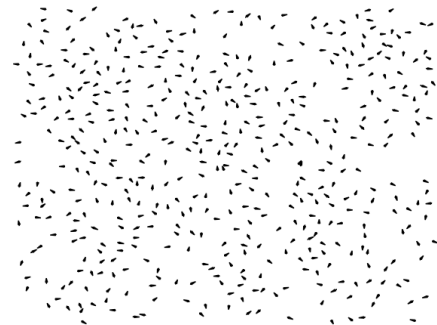
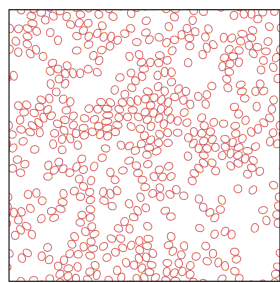
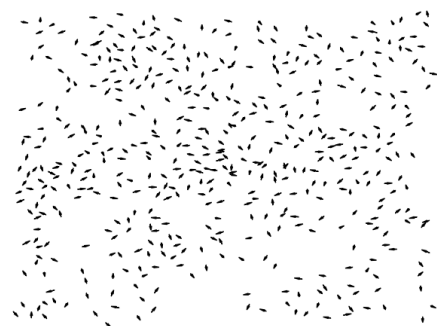
(a) $F_D = 32\frac{\epsilon}{r_b}$ (b) Velocity field for $F_D = 40\frac{\epsilon}{r_b}$

Fig. 4.2: Steady-state snapshots under Different Propulsion Forces by elongated cells

(a) $F_D = 0\frac{\epsilon}{r_b}$ (b) Velocity field for $F_D = 0\frac{\epsilon}{r_b}$ (c) $F_D = 16\frac{\epsilon}{r_b}$ (d) Velocity field for $F_D = 16\frac{\epsilon}{r_b}$ (e) $F_D = 24\frac{\epsilon}{r_b}$ (f) Velocity field for $F_D = 24\frac{\epsilon}{r_b}$

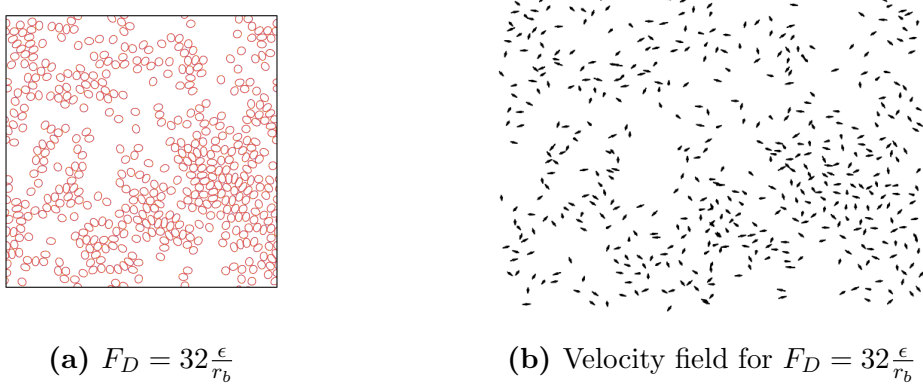


Fig. 4.4: Steady-state snapshots under Different Propulsion Forces by circular cells

To explore cooperative motion among cells, we analyze the average cluster size ($\langle m \rangle$) as a function of motility force at a fixed density ($\rho = 0.3125$). A cell is considered part of a cluster if it has at least one monomer within a distance $d \leq r_b$ from another cell. We observe a steady increase in the average cluster size with increasing motility force (F_D), indicating enhanced cooperative behaviour among cells. Notably, elongated cells tend to form larger clusters compared to circular cells at a particular motility force and density as can be seen from figure 4.2 and 4.4.

Similar phenomena are observed in self-propelled rods with short-range repulsion, as reported in previous studies [4]. The onset of clustering is marked by a transition from unimodal to bimodal cluster size distribution. Specifically, at low motility forces, the cluster distribution exhibits an exponentially decreasing trend, while at higher motility forces, there is a peak in the distribution at larger cluster sizes. When the cells show highly collective motion their cluster distribution is peaked at higher values. Figure 4.6 shows the normalised plot of the cluster distribution for different motility forces for elongated cells. In the low motility region, the cluster distribution exhibits an exponentially decreasing nature, represented by the equation:

$$p(m) \sim \exp\left(-\frac{m}{m_0}\right),$$

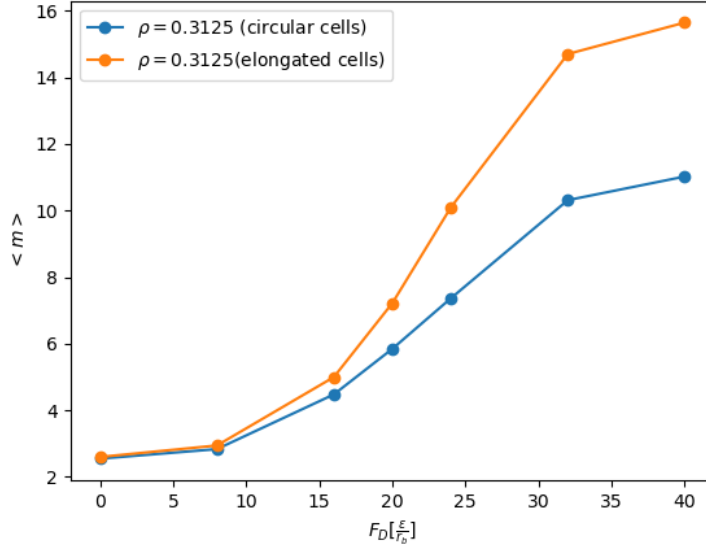


Fig. 4.5: Average cluster size $\langle m \rangle$ Vs motility force for circular cells and elongated cells and $\rho = 0.3125$

for low motility forces ($F_D \lesssim 16\frac{\epsilon}{r_b}$), which implies that there exists a characteristic cluster size. This phase is characterized by the existence of large clusters that are reflected by the emergence of a local maximum in the cluster distribution in figure 4.6. The transition is evident by the functional change displayed by $p(m)$, monotonically decreasing with m for small values of F_D , while exhibiting a shoulder at large F_D values. This also corresponds to the maximum susceptibility value of the Vicsek order parameter. In the case of higher motility force, the distribution shows a power law ($p(m) \sim m^{-\eta}$) for a long range which indicates the absence of a characteristic cluster size and emergent collective motion. For the higher value of F_D , the distribution exhibits power law with higher exponents. In our case, there is the absence of local maxima at higher cluster size as in the case of self-propelled rods[4] which can be seen in the inset of figure 4.7. Note that cluster distribution in the experiments on *Myxococcus xanthus* [3] has similar behaviour of formation of the shoulder at higher cluster size, as seen in our simulation.

The dynamic nature of cluster size within a system can be elucidated

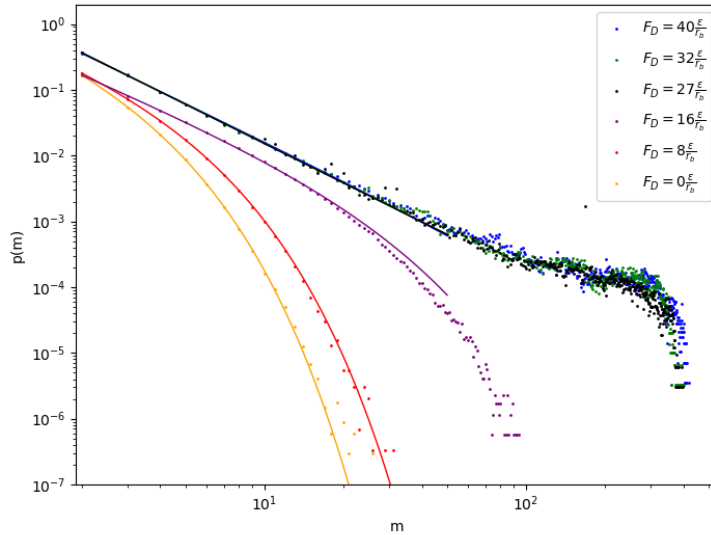


Fig. 4.6: Normalized cluster distribution of elongated cells at $\rho = 0.3125$ for various value of motility force

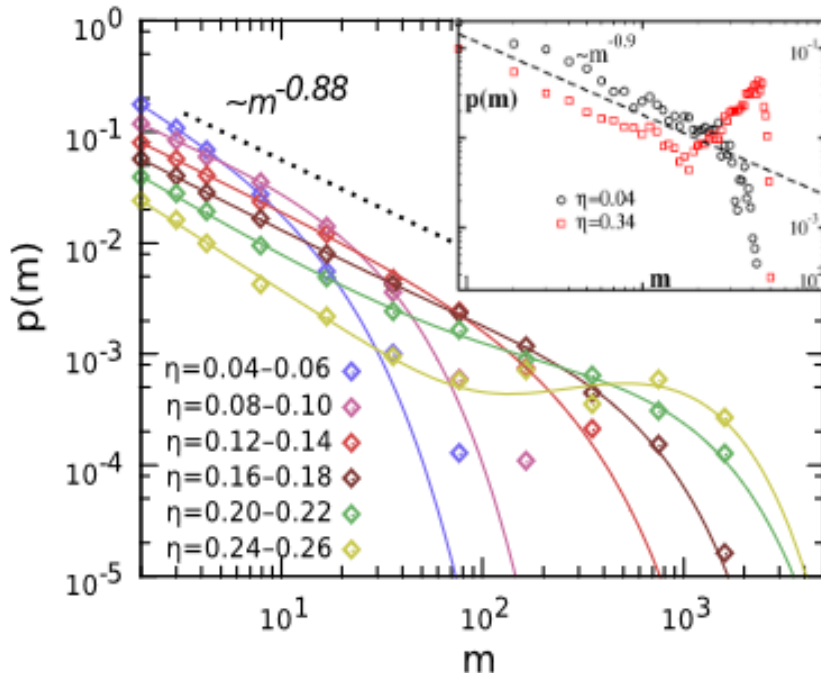


Fig. 4.7: the steady-state cluster-size distribution $p(m)$ for various packing fraction of *Myxococcus xanthus*[3] inset is for active rods[4]

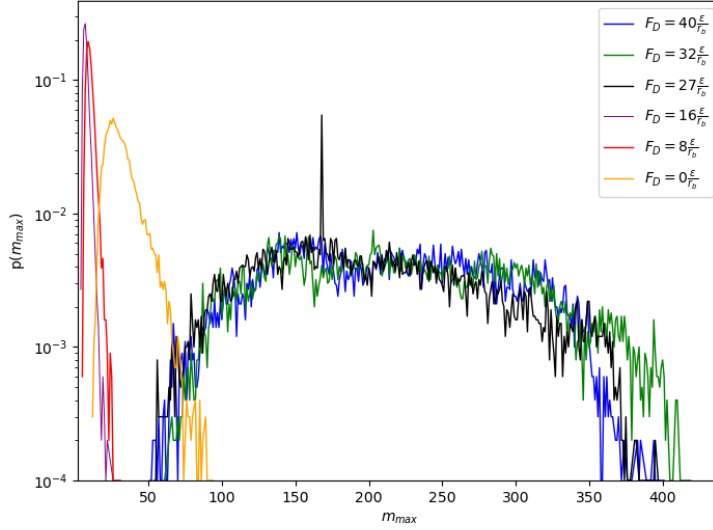


Fig. 4.8: The steady-state cluster-size distribution $p(m_{\max})$ for elongated cells.

through the analysis of the normalized distribution of maximum cluster size, denoted as m_{\max} . In this context, m_{\max} represents the instantaneous largest cluster size observed within the system at any given timestep. Each discrete timestep corresponds to a distinct value of m_{\max} , thereby offering a temporal understanding of cluster dynamics.

A key inference drawn from the distribution of m_{\max} is the degree of variability or fluctuation in cluster sizes over time. A wider distribution signifies a greater degree of variability, indicating that clusters exhibit more pronounced fluctuations in size. This suggests a dynamic and potentially unstable system where cluster configurations rapidly evolve.

Moreover, in scenarios characterized by higher motility, the distribution of m_{\max} tends to exhibit greater breadth. This phenomenon arises from the propensity for larger clusters to undergo substantial and frequent changes in configuration due to interaction. Consequently, in systems subject to higher motility forces, larger clusters display heightened dynamism, contributing to the broader distribution of maximum cluster sizes.

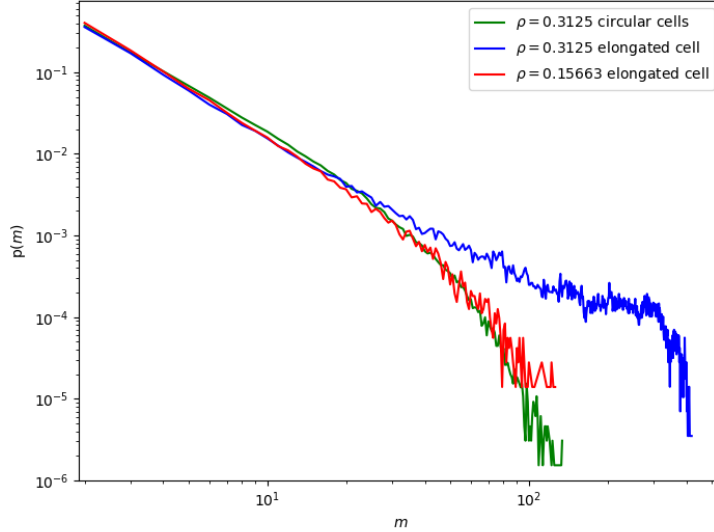


Fig. 4.9: the steady-state cluster-size distribution $p(m)$ for packing fraction ($\rho = 0.1563$ and 0.3125) elongated cells(red and blue) , circular cells (green)

The cluster size distributions of elongated cells at two different densities ($\rho = 0.1563$ and 0.3125) and high motility forces are shown in figure 4.9. These distributions exhibit qualitative differences. Specifically, at low densities, the cluster size distribution decays exponentially and lacks a shoulder even at high motility forces. This suggests that cell density also influences the emergence of collective behaviour among cells.

Furthermore, 4.9 illustrates the cluster size distribution for circular cells (green curve) at the same density and motility force as those of elongated cells where collective behaviour is observed ($\rho = 0.3125$ and $F_D = 40\epsilon/r_b$). In contrast to elongated cells, the cluster size distribution of circular cells displays a power-law behaviour at small and intermediate cluster sizes. It does not display a shoulder formation in the high cluster size region.

To quantify the emergent collective motions we consider two order parameters the first one is the vicsek order parameter which is a measure of the alignment of the velocities of the cells. It is defined as follows:-

$$S_v = \left\langle \left| \frac{1}{P} \sum_{l=1}^P \exp(i\alpha_l(t)) \right| \right\rangle_t \quad (4.1)$$

Here, $\alpha_l(t)$ represents the instantaneous angle of the cell's velocity $\mathbf{v}_l(t)$ with respect to the X-axis. P denotes the total number of cells, and the average is computed over the timesteps.

The second order parameter is the nematic order parameter which is a measure alignment of the unsigned polarity of the cells. The nematic tensor is given by:-

$$\hat{Q} = \begin{pmatrix} Q_{xx} & Q_{xy} \\ Q_{xy} & -Q_{xx} \end{pmatrix} = \alpha \begin{pmatrix} \cos(2\theta) & \sin(2\theta) \\ \sin(2\theta) & -\cos(2\theta) \end{pmatrix}$$

Defining now a unit vector (the director) \hat{n} with components $n_x = \cos \theta$ and $n_y = \sin \theta$, the nematic order parameter reads:

$$\hat{Q} = \alpha \begin{pmatrix} n_x^2 - n_y^2 & 2n_x n_y \\ 2n_x n_y & n_y^2 - n_x^2 \end{pmatrix},$$

or in component notation:

$$\hat{Q}_{ij} = 2\alpha \left(n_i n_j - \frac{1}{2} n^2 \delta_{ij} \right)$$

It can also be written in the complex notation as follows:-

$$S_p = \left\langle \left| \frac{1}{P} \sum_{l=1}^P \exp(i2\beta_l(t)) \right| \right\rangle_t \quad (4.2)$$

where $\beta_l(t)$ is the angle made by polar axis of the cells with the axis. The nematic symmetry implies that the order parameter is not a vector. It is invariant under transformation from $\beta_l(t)$ to $\beta_l(t) + \pi$ as both represent the same nematic order.

From Figure 4.10, we observe the plot of S_v against motility force for different cell configurations: elongated cells at two different densities, $\rho = 0.3125$ and $\rho = 0.1563$, and circular cells at density $\rho = 0.3125$.

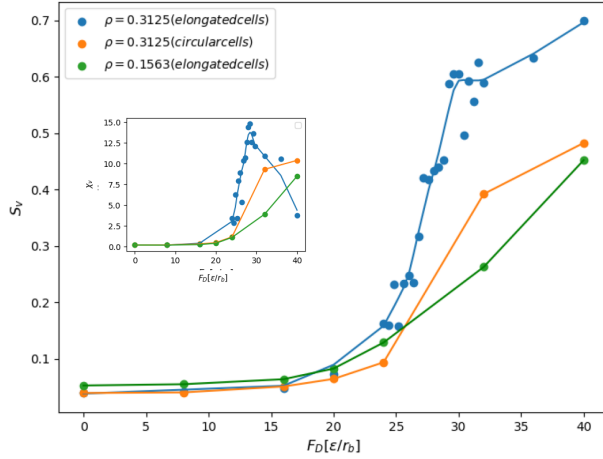


Fig. 4.10: Vicsek order parameter, calculated using motility force for the case of elongated cells with $\rho = 0.3125$, elongated cells with $\rho = 0.1563$, and circular cells with $\rho = 0.3125$. The inset shows the susceptibility of the Vicsek order parameter.

The plot reveals that the Vicsek order parameter, S_v , demonstrates a notably sharper increase in the range of motility force from $25\epsilon/r_b$ to $30\epsilon/r_b$. This indicates a pronounced enhancement in the alignment of particle velocities, suggesting a transition towards collective motion.

Moreover, it is evident that for the case of elongated cells, regardless of motility, the value of S_v is consistently higher compared to that of circular cells at $\rho = 0.3125$ and elongated cells at $\rho = 0.1563$. This signifies a greater degree of alignment and coherence among the motions of elongated cells, especially at higher densities and motility forces. Let us look at the susceptibility of the Vicsek order parameter given by,

$$\chi_v = \mathcal{P} (\langle S_v^2 \rangle_t - \langle S_v \rangle_t^2), \quad (4.3)$$

here \mathcal{P} denotes the number of cells, $\langle \cdot \rangle_t$ denotes the time average, and S_v

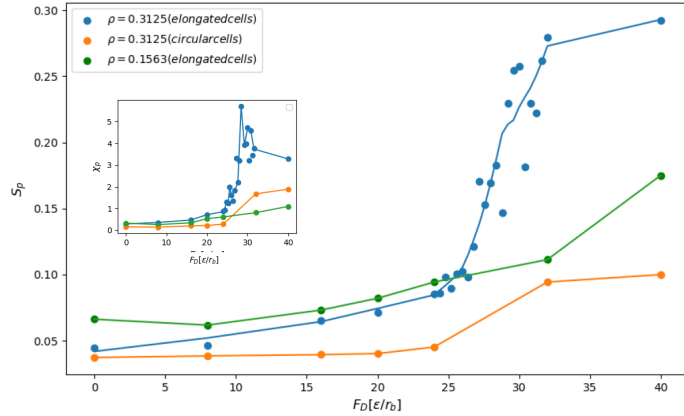


Fig. 4.11: Polar order parameter, calculated using motility force for the case of elongated cells with $\rho = 0.3125$, elongated cells with $\rho = 0.1563$, and circular cells with $\rho = 0.3125$. The inset shows the susceptibility of the Polar order parameter

represents the Vicsek order parameter. The behaviour of χ_v with respect to motility force is depicted in the inset of Figure 4.10, which exhibits a peak around $F_D \approx 27.3\epsilon/r_b$. This peak indicates the transition from disordered motion to collective motion.

Interestingly, in the case of circular cells and elongated cells at $\rho = 0.1563$, the peak is absent. Instead, there is a gradual increase in the susceptibility with the motility force. This suggests that while collective motion is not observed in these configurations at this density, there is still a progressive response of the system to increasing motility forces.

The polarity order parameter, S_p , shown in 4.11 as a function of F_D , also exhibits the same behaviour as the Vicsek order parameter, however, the amplitude of S_p is weaker compared to S_v at high values of F_D . This suggests that when cells engage in cooperative motion, the alignment of their

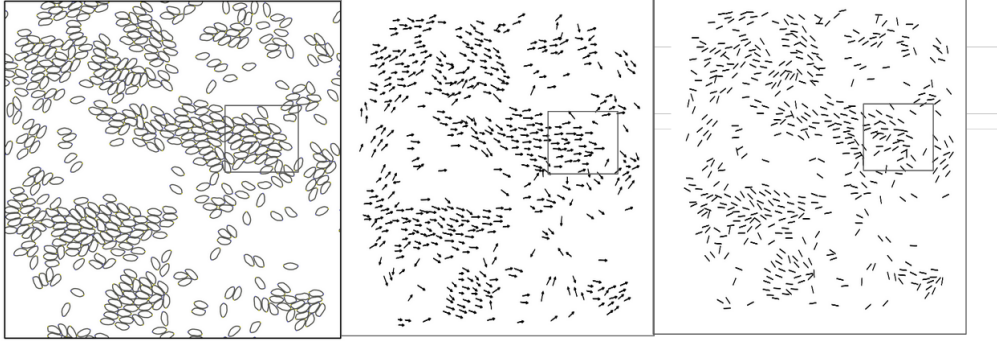


Fig. 4.12: Snapshots of cells, their velocities and their polarities respectively

velocities is stronger than that of their polarities. The inset of 4.11 reveals the susceptibility of the polarity order parameter, χ_p , for elongated cells with $\rho = 0.3125$, calculated in the same manner as χ_v . It also exhibits a peak at approximately the same motility force as χ_v around $F_D \approx 27.3\epsilon/r_b$ shown in the inset of 4.11. For the elongated cell, the polar order parameter is much less as compared to the Vicsek order parameter and the susceptibility has a less sharp peak as compared to the Vicsekorder parameter. So the Velocities of the self-propelled particles are more likely to get aligned than the polarities of the cell during the collective motion. In the figure 4.12 inside the square, the velocities are more correlated than their polarities.

We performed a simulation with constant motility force and varying the density. The results depicted in Figure 4.13 reveal a significant trend: the Vicsek order parameter increases with increasing density, particularly notable at a high motility force ($F_D = 40\epsilon/r_b$). Furthermore, this is also evidence of a transition from a disordered state at low densities to a cooperative state at higher densities.

The collective motion of self-propelled particles with short-range repulsion is a result of many-body interactions between the active particles. To study the mechanism of alignment and the role of cell elongation in the collective coherent motion, we performed a scattering experiment between two elongated cells, the angle between the cells' polarity(θ_p) and velocities(θ_v) is $\pi/2$. we consider a specific case where the motility force is kept constant at $F_D = 40\epsilon/r_b$.

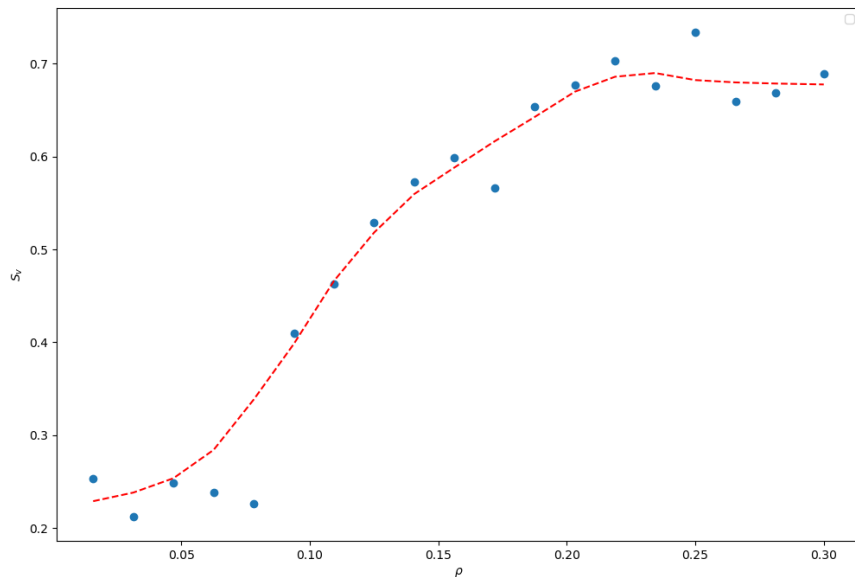


Fig. 4.13: Vicsek order parameter with density in case of elongated cells

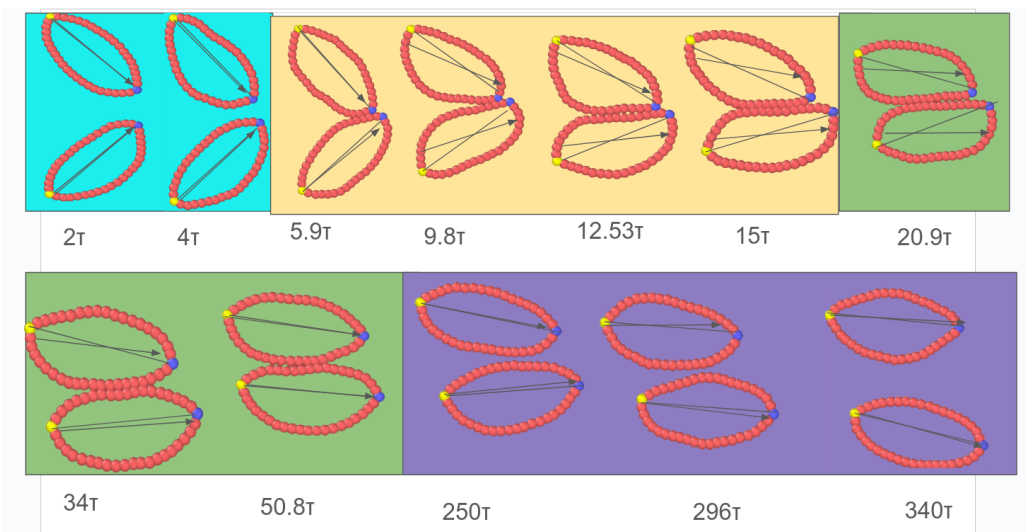


Fig. 4.14: Various stages of collision of two elongated cells, the arrows show the direction of velocities of the individual cells lines are the polar axis of the cells

In the beginning stages of collision, $(6\tau - 15\tau)$ between the cells the light yellowed coloured region in the figure shows there is deformation in the shape of the cells indicating that it is an inelastic collision and phase of both the cells start aligning together which is evident from the decrease in θ_p and θ_v however the aligning of velocities is faster than that of polarities of both the cells, by the end of this stage the velocities of both the cells got aligned but their polarities are still not aligned. This stage is called the collision stage. The longer adhesion stage is when the two cells move while remaining in contact with each other in the same direction their velocities remain aligned $(21\tau - 250\tau)$. By the end of this adhesion stage, the contact between the cells starts losing. Following by adhesion stage the two cells start polarities of the two cells get aligned Then they start separating from each other this is called the separation stage. The above Fig. 4.14 shows that the two cells can move together while their polarities can remain misaligned. The misalignment of polarities of cells makes the dimer stable and move together by pushing against each other.

We also do the same scattering experiment between two circular cells, in the case of circular cells the with same initial conditions as that of elongated cells and the same motility force $F_d = 40\epsilon/r_b$. In the case of circular cells, the adhesion stage is much shorter than that of elongated cells, during adhesion the the cells' velocities get aligned but their polarities never align. After the end of the adhesion stage, once the velocity of the individual cell gets aligned with its polarity, the two cells slip away from each other. The stability of the dimer formed between 2 cells in the case of a circular shape is much less than that of elongated cells which causes the cluster of circular cells less stable and leads to less collective motion in the case of circular cells.

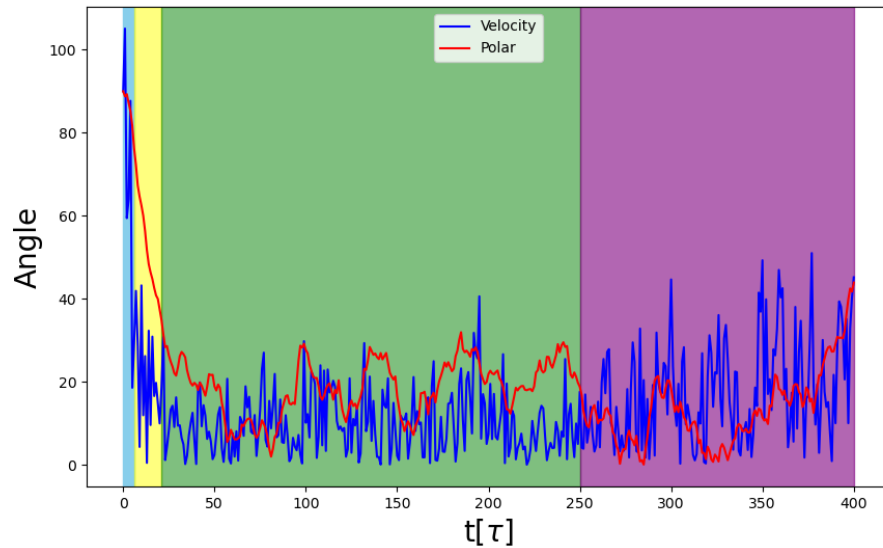


Fig. 4.15: Different background colours in the graph indicate different stages of collision, For blue is the pre-collision stage, yellow is the collision stage, green is the adhesion stage and purple is the separation stage

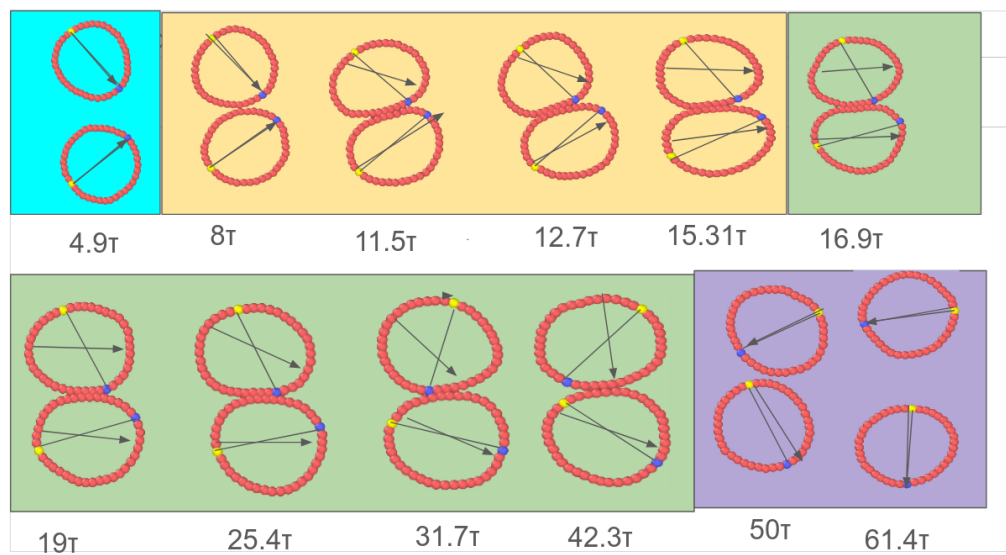


Fig. 4.16: Various stages of collision of two elongated cells, the arrows show the direction of velocities of the individual cells lines are the polar axis of the cells

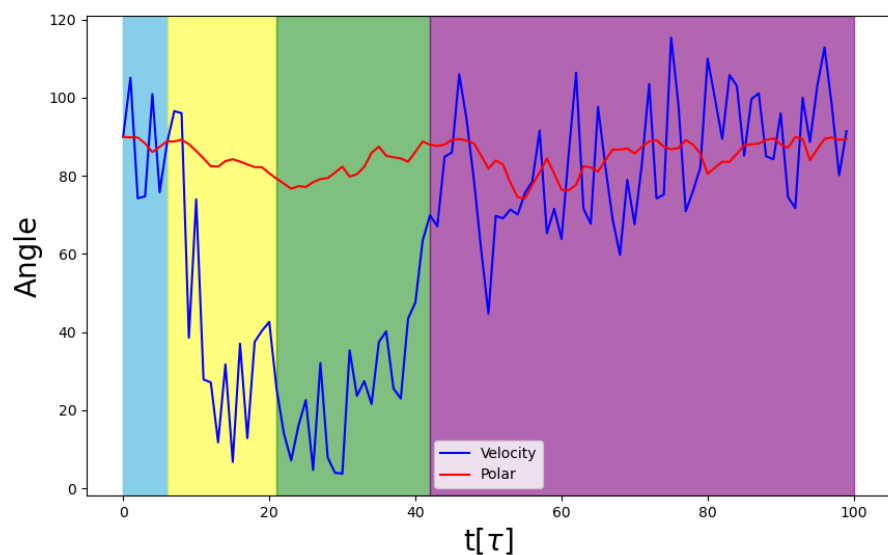


Fig. 4.17: Various stages of collision of two elongated cells, the arrows show the direction of velocities of the individual cells lines are the polar axis of the cells

Cells inside a semiflexible confinement

We now move to the confinement of active rings(2D cells) inside a semiflexible boundary. Active particles inside a semiflexible confinement show various emergent phenomena. There are experiments with bacteria confined inside a lipid vesicle and dry active particles confined to paper rings[9]. The collection of confined active particles forms a dynamic cluster and pushes against the boundary. In the case of the flexible boundary, it can lead to shape fluctuation and the formation of large curvature in the boundary and spontaneous directed motion of the whole composite system[10]. The mindless robots confined to a flexible scaffold show many emergent behaviours that the individual robots don't show. They can move through narrow passages smaller than their size, and move around obstacles, The geometry of the environment and the presence of the obstacle makes the dynamics of the composite system more richer [11].

In our case cells are confined to a circular passive semiflexible boundary, and then the dynamics of the composite system are studied by varying the density of the cells inside the boundary and the bending modulus of the boundary. The particles that make up the boundary have the same properties as the beads of the cells. The boundary is passive. In our case, the vesicle is made out of 5000 monomers, and the equilibrium bond length of the boundary was $1 r_b$, which means without any particle inside it the boundary is a circle of radius $\approx 80r_b$.

We perform a simulation varying the packing fraction inside the confinement. It is observed that for the low value of packing fraction, the cells inside the boundary show a vortical motion. As we increase the number of cells inside the boundary, there is a transition from a vortical motion to a ballistic motion. During the vortical motion, the cells can rotate either clockwise or anti-clockwise. And the angular velocity of rotation is not constant. One would naively think that the motility of the composite system will increase if we increase the number of active agents inside it, but it is more complicated as the translational motion of the vesicle gets coupled with a vortical motion. Initially, the cells are randomly oriented inside the boundary. In

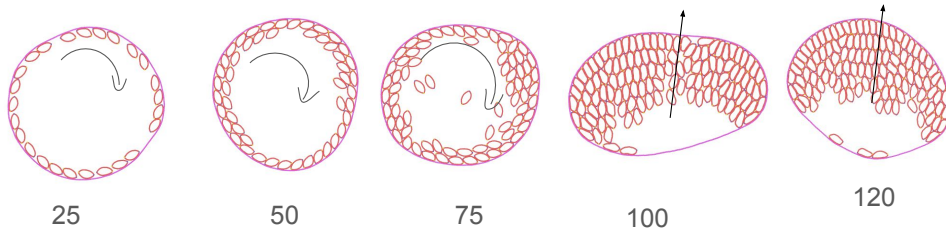


Fig. 4.18: The number below each figure indicates the number of cells inside the boundary. For the lower packing fraction, it shows vertical motion while for the higher packing fraction, it shows a persistent motion.

the case of fewer number cells, they initially show some rearrangement after that all the cells hug the boundary in the tangential direction as a result of which it shows a vortical motion. But as we increase the number of cells the vortical motion disappears and the composite system shows a directed motion where the cells get stuck to the boundary at some angle which gives rise to the persistent motion.

We also study how the motility of the composite system varies with the bending modulus of the boundary at a constant packing fraction. We put 120 cells inside the semiflexible boundary and varied the bending stiffness of it.

Active particles confined to rigid and curved confinement accumulate at the boundary [12]. Since the vesicle is flexible one expects to increase in the curvature of the regions of the boundary, where the active particle accumulates, in turn, it also causes the other to accumulate at that high curvature region. One may think that in the low-stiffness case, the active particles are more likely to form such curvature which leads to an elongated shape of the

confining space, causing a persistent motion, and in the high-stiffness case there would be a uniform distribution of active particles along the boundary causing less motility to the composite system.

For all values of the bending modulus, the composite system initially undergoes some rearrangement of the cells inside it. Subsequently, it exhibits ballistic motion, as evident from the plots (4.19). The time required for rearrangement is shorter for lower bending modulus values, whereas it takes longer for systems with higher bending modulus boundaries. In the long-time regime, the motion does not conform to a diffusive pattern. The coupling between the rotation of the composite system and its translational motion complicates its behaviour. Observing the mean squared displacement (MSD) plots in fig.(4.19), we notice non-uniform fluctuations in the long timescale, possibly indicating quasi-periodic circular or helical motion. In the case of a fully flexible boundary, such motion is less prominent, but there is sustained directed motion for a significant duration. For softer boundaries, the deformation in its shape is larger as compared to the stiffer boundary. For active rods[13] there exists an optimal thickness for which the motility is maximum. But in this scenario, the motility is almost independent of the bending modulus of the boundary.

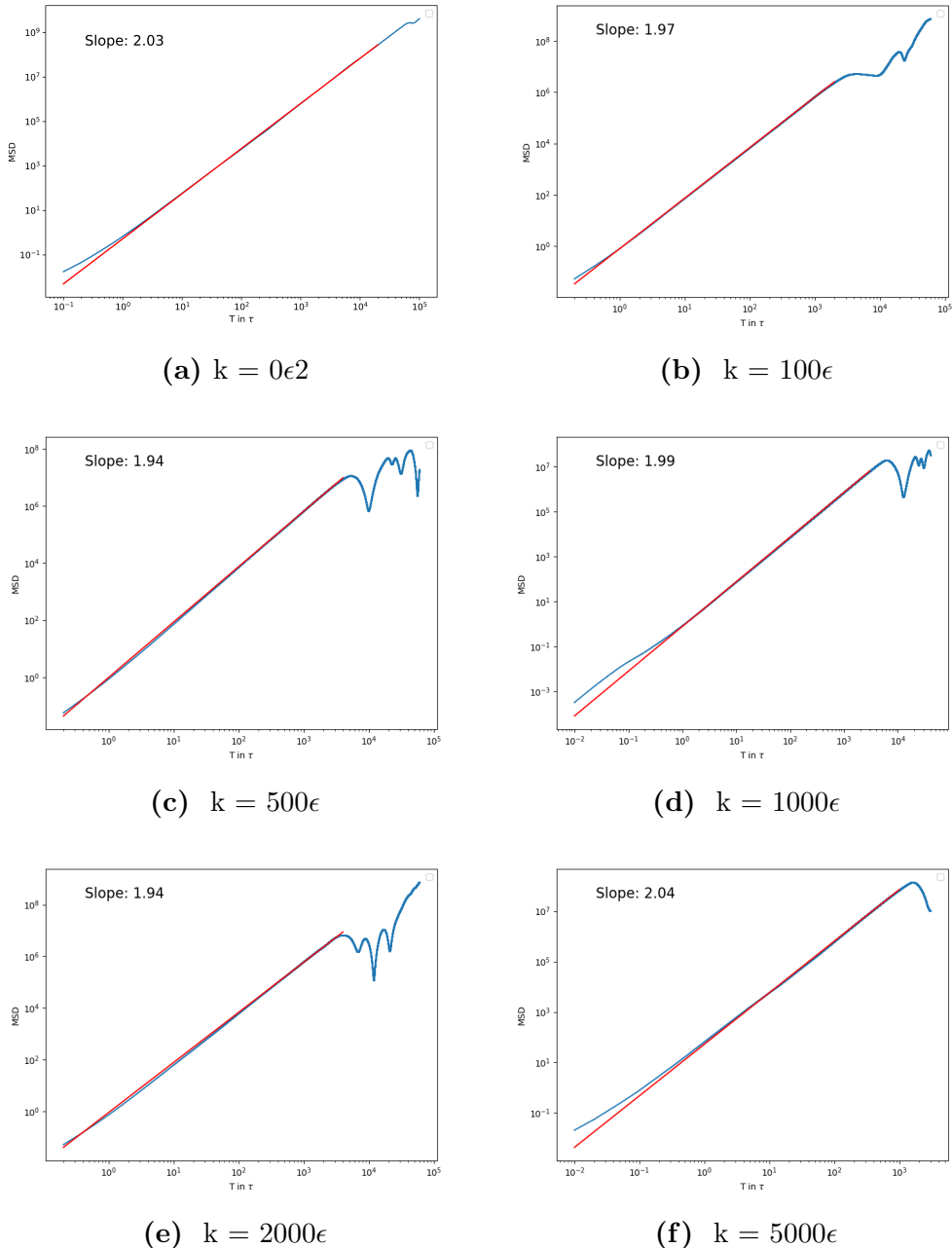


Fig. 4.19

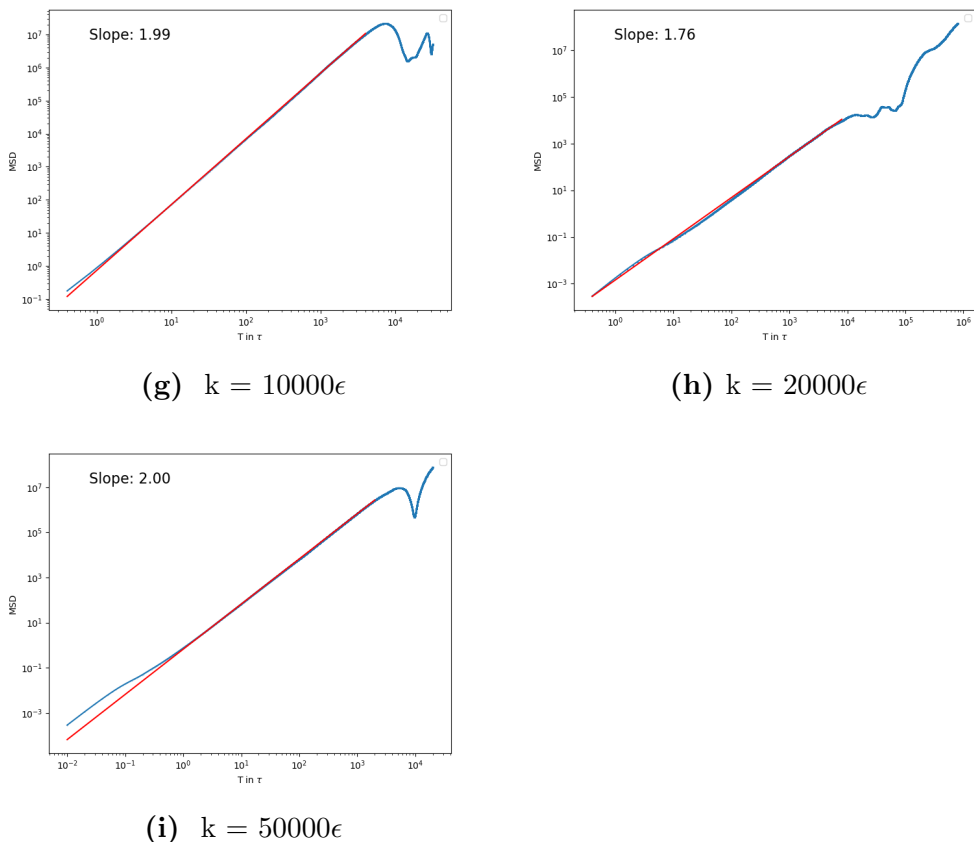


Fig. 4.19: MSD plot of the confined active particles with time for various values of the bending modulus of the boundary

5. SUMMARY AND OUTLOOK

A cell is modelled as a semiflexible ring polymer, incorporating both its semiflexibility and area constraints into the model. To give an elongated shape to the cell, a preferred angle of $\theta_p = 120^\circ$ is introduced at the two poles. This shape anisotropy leads to the collective motion at high density and motility force.

In simulations, elongated cells exhibit more pronounced collective motion compared to circular cells. The shape anisotropy of the elongated cells facilitates this collective behaviour, which is less evident in circular cells. The distribution of cell clusters displays distinct characteristics depending on the motility force. In the low motility force regime, the cluster size distribution follows an exponential decay pattern. Conversely, at high motility forces, the distribution exhibits a power law with shoulder formation for higher cluster sizes, indicating the presence of larger clusters.

The dynamics of the system are further analyzed using the Vicsek order parameter and the polar order parameter. Both parameters show a peak in susceptibility at $F_D = 27.3\epsilon/r_b$, indicating a critical point for collective motion. However, the peak in the Vicsek order parameter is higher than that in the polar order parameter. This suggests that during collective motion, the velocities of individual cells are more likely to align than their polarities. The Vicsek order parameter shows a consistent increase in density. I also conducted a scattering experiment where two cells come together and deform each other's shapes. Then, their velocities aligned, causing them to move together. After their polarities align, they started separating from each other. For circular cells, they move together for a very short time before slipping apart.

In this study, we did not investigate the impact of noise on the collective

motion of cells. Exploring the effect of noise on collective motion may give useful insights.

The dynamics of a number of cells under semiflexible confinement was investigated by varying the packing fraction inside a semiflexible boundary. Distinct motion patterns of confined cells were observed: at low packing fractions, cells exhibit vortical motion, rotating either clockwise or anti-clockwise with variable angular velocity. As the number of cells increases, this motion transitions to ballistic and directed motion.

Regardless of the bending modulus, the system undergoes initial cell rearrangement, with shorter rearrangement times for lower bending modulus and longer times for higher bending modulus. Subsequently, the system exhibits directed ballistic motion, but over long timescales, it deviates from a diffusive nature.

BIBLIOGRAPHY

- [1] Guanming Zhang, Romain Mueller, Amin Doostmohammadi, and Julia M. Yeomans. Active inter-cellular forces in collective cell motility. *J. R. Soc. Interface*, 17(20200312), 2020.
- [2] Satoru Okuda, Yasuhiro Inoue, Mototsugu Eiraku, Yoshiki Sasai, and Taiji Adachi. Reversible network reconnection model for simulating large deformation in dynamic tissue morphogenesis. *Biomechanics and Modeling in Mechanobiology*, 12(4):627–644, August 2013.
- [3] Fernando Peruani, Jörn Starruß, Vladimir Jakovljevic, Lotte Søgaard-Andersen, Andreas Deutsch, and Markus Bär. Collective motion and nonequilibrium cluster formation in colonies of gliding bacteria. *Phys. Rev. Lett.*, 108:098102, Feb 2012.
- [4] Fernando Peruani, Andreas Deutsch, and Markus Bär. Nonequilibrium clustering of self-propelled rods. *Phys. Rev. E*, 74:030904, Sep 2006.
- [5] Tamás Vicsek, András Czirók, Eshel Ben-Jacob, Inon Cohen, and Ofer Shochet. Novel type of phase transition in a system of self-driven particles. *Phys. Rev. Lett.*, 75:1226–1229, Aug 1995.
- [6] LAMMPS Molecular Dynamics Simulator.
- [7] Haosheng Wen, Yu Zhu, Chenhui Peng, P. B. Sunil Kumar, and Mohamed Laradji. Collective motion of cells modeled as ring polymers. *Soft Matter*, 18:1228–1238, 2022.
- [8] Mario Theers, Elmar Westphal, Kai Qi, Roland G. Winkler, and Ger-

- hard Gompper. Clustering of microswimmers: interplay of shape and hydrodynamics. *Soft Matter*, 14:8590–8603, 2018.
- [9] Pragya Arora, Souvik Sadhukhan, Saroj Kumar Nandi, Dapeng Bi, AK Sood, and Rajesh Ganapathy. A shape-driven reentrant jamming transition in confluent monolayers of synthetic cell-mimics. *arXiv preprint arXiv:2401.13437*, 2024.
 - [10] Matteo Paoluzzi, Roberto Di Leonardo, M. Cristina Marchetti, and Luca Angelani. Shape and displacement fluctuations in soft vesicles filled by active particles. *Scientific Reports*, 6(1):34146, 2016.
 - [11] J. F. Boudet, J. Lintuvuori, C. Lacouture, T. Barois, A. Deblais, K. Xie, S. Cassagnere, B. Tregon, D. B. Brückner, J. C. Baret, and H. Kellay. From collections of independent, mindless robots to flexible, mobile, and directional superstructures. *Science Robotics*, 6(56):eabd0272, 2021.
 - [12] Haosheng Wen, Yu Zhu, Chenhui Peng, P. B. Sunil Kumar, and Mohamed Laradji. Collective vortical motion and vorticity reversals of self-propelled particles on circularly patterned substrates. *Phys. Rev. E*, 107:024606, Feb 2023.
 - [13] Sarvesh Ulap, Michael F. Hagan, and Aparna Baskaran. Design principles for transporting vesicles with enclosed active particles(a). *Euro-physics Letters*, 143(6):67001, oct 2023.